PHYSICAL REVIEW D **108,** 043036 (2023)

Detection and parameter estimation challenges of type-II lensed binary black hole signals

Aditya Vijaykumar,[1] Ajit Kumar Mehta,[2,4] and Apratim Ganguly[3,1]
[1]International Centre for Theoretical Sciences (ICTS), Tata Institute of Fundamental Research,
Bangalore 560089, India
[2]Max Planck Institute for Gravitational Physics (Albert Einstein Institute),
Am Mühlenberg 1, Potsdam 14476, Germany
[3]Inter-University Centre for Astronomy and Astrophysics (IUCAA),
Post Bag 4, Ganeshkhind, Pune 411 007, India
[4]Department of Physics, University of California, Santa Barbara, California 93106, USA

(Received 30 March 2022; accepted 6 August 2023; published 30 August 2023)

Strong lensing of gravitational-wave signals can produce three types of images, denoted as type-I, type-II, and type-III, corresponding to the minima, saddle, and maxima, respectively, of the lensing potential of the lensed images. Type-II images, in particular, receive a nontrivial phase shift of $\pi/2$. This phase shift can introduce additional distortions in the strains produced by the type-II image of the binary black hole signals depending on the morphology of the signals, e.g., when they have contributions from higher harmonics, precession, eccentricity, etc. The probability of observing type-II images is nearly the same as that of strong lensing itself, and, thus, these signals are likely to be observed in the near future. In this work, we investigate the potential applicability of these distortions in helping identify type-II signals from a single detection and the systematic biases that could arise in the inference of parameters if they are recovered with gravitational-wave templates that do not take the distortion into account. We show that the lensing distortions will allow us to confidently identify the type-II images for highly inclined binaries: At network signal-to-noise ratio (SNR) $\rho = 20(50)$, individual type-II images should be identifiable with ln Bayes factor $\ln\mathcal{B} > 2$ for inclinations $\iota > 5\pi/12(\pi/3)$. Furthermore, based on the trends we observe in these results, we predict that, at high SNRs ($\gtrsim 100$), individual type-II images would be identifiable even when the inclination angle is much lower ($\sim\pi/6$). We then show that neglecting physical effects arising from these identifiable type-II images can significantly bias the estimates of source parameters (such as sky location, distance, inclination, etc.). Thus, in the future, using templates that take into account the lensing deformation would be necessary to extract source parameters from type-II lensed signals.

DOI: 10.1103/PhysRevD.108.043036

I. INTRODUCTION

The sensitivities of the LIGO and Virgo gravitational-wave (GW) detectors [1,2] are constantly improving. So far, they have already confidently detected 90 compact binary merger events [3] and are expected to detect hundreds of such mergers in the upcoming observing runs [4]. Accurate extraction of source parameters from these mergers is essential to interpret them in an astrophysical and cosmological context. Understanding and modeling physical effects due to the propagation of the wave between the source and the detector is significant in this regard. Ignoring these effects in the templates used to search and estimate parameters of a GW signal could cause problems in explaining or interpreting the underlying signals.

One such propagation effect is gravitational lensing. GWs get lensed when the signals encounter mass inhomogeneities during their journey to the detectors. If the intervening object is sufficiently massive, it can produce multiple images of the source through strong lensing [5,6]. The multiple images would differ in their magnifications and arrival times at the observer. The probability (quantified by the optical depth) for strong lensing is, however, small, e.g., $\sim 10^{-3} - 10^{-4}$ for galaxy lenses [7], mainly because it requires a strong alignment between the source, lens, and observer. Searches in GW data have not detected signatures of strong lensing so far [8,9]. Nevertheless, at the design sensitivities of Advanced LIGO and Virgo [10,11], $1.3^{+0.6}_{-0.4}$–$1.7^{+0.9}_{-0.6}$ detections of binary black holes (BBHs) lensed by galaxies are expected per year [12]. These prospects will only be enhanced with the addition of KAGRA [13,14] and LIGO-India [15,16] to the detector network. Furthermore, third-generation GW detectors like Cosmic Explorer [17] and Einstein Telescope [18] are expected to have an order of magnitude better sensitivity as compared to the current generation of detectors, thus potentially observing hundreds of thousands of mergers every year. This suggests an exciting time for doing science with strongly lensed GWs in the future [19–24].

In the geometric-optics limit, the lens equation picks solutions at extremal points of the time-delay (arrival time with respect to a reference time) surface over a family of trajectories. The images thus produced due to strong lensing can be of different types corresponding to the minima, saddle point, and the maxima of the time delay, called type-I, type-II, and type-III images, respectively. Type-I and type-III images have positive parity (i.e., positive magnification), while type-II images have negative parity. In addition, type-II images receive a $\pi/2$ phase shift, while type-I and type-III images receive a phase shift of 0 and π, respectively [25]. Thus, unlensed signals with an overall magnification can mimic type-I and type-III images. On the other hand, type-II images get distorted compared to their unlensed counterparts due to the nontrivial phase shift of $\pi/2$. In the cases when the GW radiation is mainly composed of the dominant harmonics ($2, \pm 2$ modes), these distortions can be mimicked by type-I or the unlensed GW signals by adjusting their parameters, such as the coalescence phase and/or polarization angle [26]. However, when the signal has significant contributions from higher harmonics, precession, or eccentricity, these distortions may not be reproduced by the type-I signals [26], as also discussed in Sec. II here. In such cases, the current strategies that LIGO-Virgo follows, i.e., analyzing a detected signal under the hypothesis that the signal is unlensed, may lead to significant biases in the inferences of the parameters. The standard LIGO-Virgo search pipelines could also miss the signals [7,26].

Under the singular isothermal ellipse approximation[1] for the galaxy lenses [27], it has been shown that the probability of seeing multiple images without a type-II image being one of them is less than 0.01% [7]. Hence, the probability of observing type-II images is practically the same as that of strong lensing. Moreover, it was also shown that more than 90% of sources with multiple images would have a type-II image as the second brightest image [7]. Thus, if a strongly lensed event pair is detected, there is a high chance that a type-II image would be present.

In this work, we thoroughly investigate the systematic effects that could arise when a type-II lensed (BBH) signal is recovered with the type-I and unlensed templates. We first establish the cases where a single-event-based confident identification of the type-II nature of a signal could be possible. This is done by choosing a threshold for the ln Bayes factor between the two hypotheses **A** and **B**, where **A** represents the hypothesis where we inject a type-II signal and recover with type-II templates, and **B** represents the hypothesis when the type-II injected signal is recovered with the type-I template. We claim a type-II signal is identified when the ln Bayes factor $\ln \mathcal{B} \geq 2$. We study the effect of strong lensing on a broad set of injections at a total signal-to-noise ratio (SNR) of 20 and 50, using the noise spectra of the LIGO-Virgo design sensitivities. We show that, even at modest values of SNR, the type-II nature of the image can be inferred for moderate to high values of the inclination angle. We also show that noninclusion of the $\pi/2$ phase shift in the parameter estimation templates for such signals could lead to significant systematic errors, rendering the recovered posteriors inconsistent with the true values. In other words, the parameters of the signals could be wrongly inferred if type-II templates are not used during the parameter estimation (PE). This could, in turn, bias the astrophysical interpretation of the source—e.g., a lighter BH could be wrongly attributed to higher mass—thus causing difficulties in explaining their formation mechanisms.

One strategy to look for the strong lensing signatures in the data is by analyzing pairs of events with consistent sky locations and chirp masses [28,29].[2] This is motivated by the belief that strong lensing will not affect the frequency profile of the observed signal. This is indeed true for type-I and type-III images and, in some cases, even for the type-II images if they are quasicircular and contain only the dominant (22) mode. In general, though, one would need to perform a joint analysis, where a pair of events are simultaneously analyzed [31–33]. However, as we discussed before, in a realistic scenario, if there is a lensed event pair in the data, one of them would likely be a type-II image. Then, given that we would not know *a priori* the parameters of the underlying unlensed GW signal, we may not expect that there will be consistency in the parameters (such as the chirp mass and the sky location parameters) extracted using the templates of the unlensed signals. Thus, in principle, one would need to do a joint-PE search over the full data without any prior belief. This may become a difficult task for such techniques, given their computational costs. On the other hand, doing a full search over data for just the individual type-II images should be relatively easy, and, if detected, they can help narrow down the search for its corresponding pair, since we would already know the parameters of the underlying unlensed signal. Moreover, when the lensed pair cannot be detected due to detector downtime or data quality issues, lensing signatures can be obtained from just one image and further used for downstream analyses such as estimating lensing rates.

We note that a similar study has been performed in Ref. [7]. However, the study therein is based on the analytical approximation of the Bayes factor, emphasizing the identification of the type-II signals. They also do not explicitly consider the detector response of the GW signals, avoiding this by assuming that both polarizations are

---

[1] A more realistic approximation than the singular isothermal sphere.

[2] Reference [30] quantifies the false alarm probabilities associated with this strategy and the difficulties that arise in the identification of lensed events as a result.

measurable. In our work, we perform a full parameter estimation study, emphasizing both the identification of the type-II signals and the biases in the inference of the binary parameters. Thus, in this sense, our work builds upon their work along with this particular goal. We also note that Ref. [34] has performed a complementary analysis, showing that including higher-order modes in joint PE allows identifying of individual image types in a lensed pair.

This paper is organized as follows: In Sec. II, we explain the effect of the strong lensing on GWs and describe the method followed in this work. In Sec. III, we discuss the results based on a wide set of simulations tuned to our interests. Section IV presents the conclusion and future work.

II. SETUP

A. Theory

The problem of lensing of GWs has been looked at in depth already [35]. In geometric optics limit (i.e., the short-wavelength regime, valid for, e.g., lensing of GWs by galaxies), the effect of lensing on GWs can be derived from the Kirchhoff diffraction integral[3] by choosing points on the image plane corresponding to the extremal points of the time delay [36]. Since the extremal points can be either the minimum, saddle, or maximum, we can have three types of images: type-I, type-II, and type-III, respectively. In this limit, the Kirchhoff integral reduces to the Gaussian integral around these extremal points, and the result is the following amplification factor for the jth image:

$$F_j(f) = \sqrt{\mu_j}\exp[2\pi i f \delta t_j - \mathrm{sgn}(f) i n_j \pi], \qquad (1)$$

where f is the observed GW frequency, μ_j and δt_j represent the magnification and time delay, respectively, of the jth image, and the extra phase shift $\Delta\phi_j = \mathrm{sgn}(f) n_j \pi$ results from the integration of the complex Gaussian function, where n_j, called the Morse index, takes the values 0, 1/2, or 1 for type-I, -II, or -III images, respectively. The lensed GW signal is then given by convolving the unlensed signal with the amplification factor:

$$\tilde{h}^L_{+,\times,j}(f) = F_j(f)\tilde{h}_{+,\times}(f). \qquad (2)$$

As we can see, the type-I image receives just a linear phase compared to the unlensed signal. This linear phase is practically unimportant for all of our purposes, since this cannot be measured by the PE. The type-III image receives an additional overall negative sign but otherwise is again the same as the unlensed signal. The type-II image, on the other hand, depending on the sign of the frequencies, can receive $+\pi/2$ or $-\pi/2$ phase shifts. As a consequence, the time-domain lensed signal is given by the Hilbert transformation of Eq. (2) rather than the simple inverse Fourier transformation of the unlensed signal:

$$h^{L,\mathrm{II}}_{+,\times}(t) = -\int_{-\infty}^{\infty} df \,\mathrm{sgn}(f) i e^{-i2\pi f t}\tilde{h}_{+,\times}(f). \qquad (3)$$

For our purpose in this work, we directly use Eq. (2) for the lensed template construction, because the GW data analysis is done in the frequency domain itself. Nevertheless, Eq. (3) serves a better purpose for the visual inspections of the lensing effects, and, thus, we use it just for the sake of demonstrations. Also, the standard GW data analysis employs only the positive frequencies, because, for a real signal, the negative frequencies do not provide any extra information, and, hence, only the $+\pi/2$ phase shift is relevant for us. We now discuss the implications of the $\pi/2$ phase shift for the type-II images with different structures.

A general GW can have different harmonic contents. One way to visualize it is via spherical mode decomposition:

$$h_+(t) - i h_\times(t) = \sum_{\ell\geq 2}\sum_{m=-\ell}^{\ell} h_{\ell m}(t;\boldsymbol{\lambda})\,{}_{-2}Y_{\ell m}(\iota,\phi_c), \qquad (4)$$

where ${}_{-2}Y_{\ell m}$ [37] denotes the spin-2 weighted spherical harmonics which are function of the inclination angle[4] ι and the coalescence phase ϕ_c. The spherical harmonics basically separate the angular part of the GW radiation from its radial part, and, thus, the modes $h_{\ell m}(t)$ depend just on the intrinsic parameters ($\boldsymbol{\lambda}$) of the binary, e.g., component masses ($m_{1,2}$) and spins ($\chi_{1,2}$) if the binary is circular. For nonprecessing BBH binaries in circular motion, the $m < 0$ modes are related to the $m > 0$ due to the reflection symmetry of the GW radiation about the binary plane:

$$h_{\ell,-m} = (-1)^\ell h^*_{\ell m}. \qquad (5)$$

This helps simplify Eq. (4) in terms of only the $m > 0$ modes, and, thus, throughout this paper we use $m > 0$ modes to denote the full mode contents. On a bit further simplification of Eq. (4), writing $h_{\ell m} = A_{\ell m} e^{i\phi_{\ell m}}$, one would obtain (see Appendix C in Ref. [38])

$$h_+(t) = \sum_{\ell\geq 2}\sum_{m\geq 0} f^+_{\ell m}(\iota) A_{\ell m}(t)\cos[\phi_{\ell m}(t) + m\phi_c], \qquad (6)$$

$$h_\times(t) = \sum_{\ell\geq 2}\sum_{m\geq 0} f^\times_{\ell m}(\iota) A_{\ell m}(t)\sin[\phi_{\ell m}(t) + m\phi_c], \qquad (7)$$

where $f^+_{\ell m}(\iota)$ and $f^\times_{\ell m}(\iota)$ are functions of the inclination angle encoding the magnitude of the spherical harmonics ${}_{-2}Y_{\ell m}(\iota)$. Their explicit expressions are not relevant for the discussion here. The relative contribution of the modes ℓm to the polarizations $h_{+,\times}$ depends on the specific choice of the parameter $\boldsymbol{\lambda}$ and the inclination angle (ι). For example,

---

[3] The Kirchhoff diffraction integral describes the generic lensing phenomenon.

[4] The angle between the total angular momentum $\vec{\boldsymbol{J}}$ of the binary and the observer.

for nonprecessing BBH binaries with even the moderate mass ratio $q = m_1/m_2 \geq 4$, the contribution of higher-order modes (HMs) becomes significant, neglecting which can have consequences for detection and parameter estimation, e.g., systematic bias, loss in the detection volume, etc. [39–41].

When a GW signal reaches the detectors, the strain induced on a particular detector is given by

$$h = F_+(\theta, \phi, \psi)h_+(t) + F_\times(\theta, \phi, \psi)h_\times(t), \tag{8}$$

where F_+ and $F_\times$ are called the antenna pattern functions, which arise as a result of the detector's response to the GW signal. They represent the angular sensitivity of that detector and, hence, are functions of the sky angles θ and ϕ in the detector frame; these parameters denote the location of the binary in the sky. The angle ψ denotes the freedom in fixing the binary plane with respect to the detector plane and is called the polarization angle. The explicit expressions of the antenna pattern functions for the LIGO and Virgo detectors are[5]

$$F_+ = \frac{1}{2}[1+\cos^2(\theta)]\cos(2\phi)\cos(2\psi) - \cos(\theta)\sin(2\phi)\sin(2\psi), \tag{9}$$

$$F_\times = \frac{1}{2}[1+\cos^2(\theta)]\cos(2\phi)\cos(2\psi) + \cos(\theta)\sin(2\phi)\cos(2\psi). \tag{10}$$

By combining Eqs. (6)–(8), one would obtain

$$h = \sum_{\ell\geq 2}\sum_{m\geq 0}\mathcal{A}_{\ell m}(t)\cos[\phi_{\ell m}(t) + m\phi_c - \chi_{\ell m}], \tag{11}$$

where

$$\chi_{\ell m} = \tan^{-1}\left(\frac{F_\times(\theta,\phi,\psi)f^\times_{\ell m}(\iota)}{F_+(\theta,\phi,\psi)f^+_{\ell m}(\iota)}\right), \tag{12}$$

$$\mathcal{A}_{\ell m}(t) = A_{\ell m}(t)|F_+|[1+\tan^2(\chi_{\ell m})]^{1/2}. \tag{13}$$

Equation (11) is just a bit more simplified version of Eq. (8). Now, by taking the Fourier transform of the above equation and then applying the Hilbert transformation in Eq. (3), one can easily show that the strains produced by the lensed signals in the time domain are given as follows.

For type-I images, there is only an additional magnification factor μ_I, i.e.,

$$h_\mathrm{I} = \sum_{\ell\geq 2}\sum_{m\geq 0}|\mu_\mathrm{I}|^{1/2}\mathcal{A}_{\ell m}(t_\mathrm{I})\cos[\phi_{\ell m}(t_\mathrm{I}) + m\phi_c - \chi_{\ell m}]. \tag{14}$$

For type-II images, there is an additional $\pi/2$ phase shift:

$$h_\mathrm{II} = \sum_{\ell\geq 2}\sum_{m\geq 0}|\mu_\mathrm{II}|^{1/2}\mathcal{A}_{\ell m}(t_\mathrm{II}) \times \cos[\phi_{\ell m}(t_\mathrm{II}) + m\phi_c - \chi_{\ell m} + \pi/2], \tag{15}$$

while, for type-III images,

$$h_\mathrm{III} = \sum_{\ell\geq 2}\sum_{m\geq 0}|\mu_\mathrm{III}|^{1/2}\mathcal{A}_{\ell m}(t_\mathrm{III}) \times \cos[\phi_{\ell m}(t_\mathrm{III}) + m\phi_c - \chi_{\ell m} + \pi], \tag{16}$$

where $t_j = t + \delta t_j$ for image type $j \in \{\mathrm{I}, \mathrm{II}, \mathrm{III}\}$. As expected, the type-I and type-III induced strains are just the rescaled versions of the ones caused by the unlensed GW signals. The extra π phase shift in the type-III strains which causes just a global sign flip can be easily mimicked by the polarization angle ψ through the $\chi_{\ell m}$ term under the change $\psi \to \psi + \pi/2$. Thus, for type-III image signals, the PE with unlensed GW templates would yield a bias in the polarization angle by $\pi/2$.

The type-II induced strain is interesting, since the $\pi/2$ phase shift cannot be easily absorbed into other known parameters unless the signal is quasicircular, nonprecessing, and comprised of just the dominant $\ell m = 22$ mode, in which case the coalescence angle ϕ_c can easily absorb it by adjusting itself, $\phi_c \to \phi_c + \pi/4$, as should be clear from Eq. (15) when $m = 2$. One can note, however, that the polarization angle ψ can also try to adjust itself such that $\Delta\chi_{\ell m} = -\pi/2$, and, thus, it is not always the case that only ϕ_c will get biased during the PE as we will show later. When HMs also start contributing to the strain, the different ℓm modes would require different shifts in the ϕ_c, i.e.,

$$\phi_c \to \phi_c + \frac{\pi}{2m} \tag{17}$$

in order to mimic the $\pi/2$ lensing phase shift. Thus, the strain produced by type-II image signals would look distorted compared to its unlensed counterpart. Figure 1 (bottom panel) shows an illustrative example of this case with the binary parameters $M = 100M_\odot$, $q = 7$, and $\iota = \pi/3$. Since the inclination and the mass ratio are high here, HMs also contribute significantly, and, thus, there are additional distortions that are not mimicked by the change in the coalescence phase. However, we also show the case with the zero inclination for the same binary configuration in the top panel. For very small inclinations, the GW signals mainly contain the 22 mode, and, thus, we can see that the general relativity (GR) signal with the transformation $\phi_c \to \phi_c + \pi/4$ very well mimics the type-II image, as expected.

We now explore how helpful these distortions in the type-II image strains can be in separating such signals from a catalog of detected BBH events and, at the same time, how they would affect the inference of parameters if the

---

[5] These expressions hold when the sky angles are specified in the detector frame.

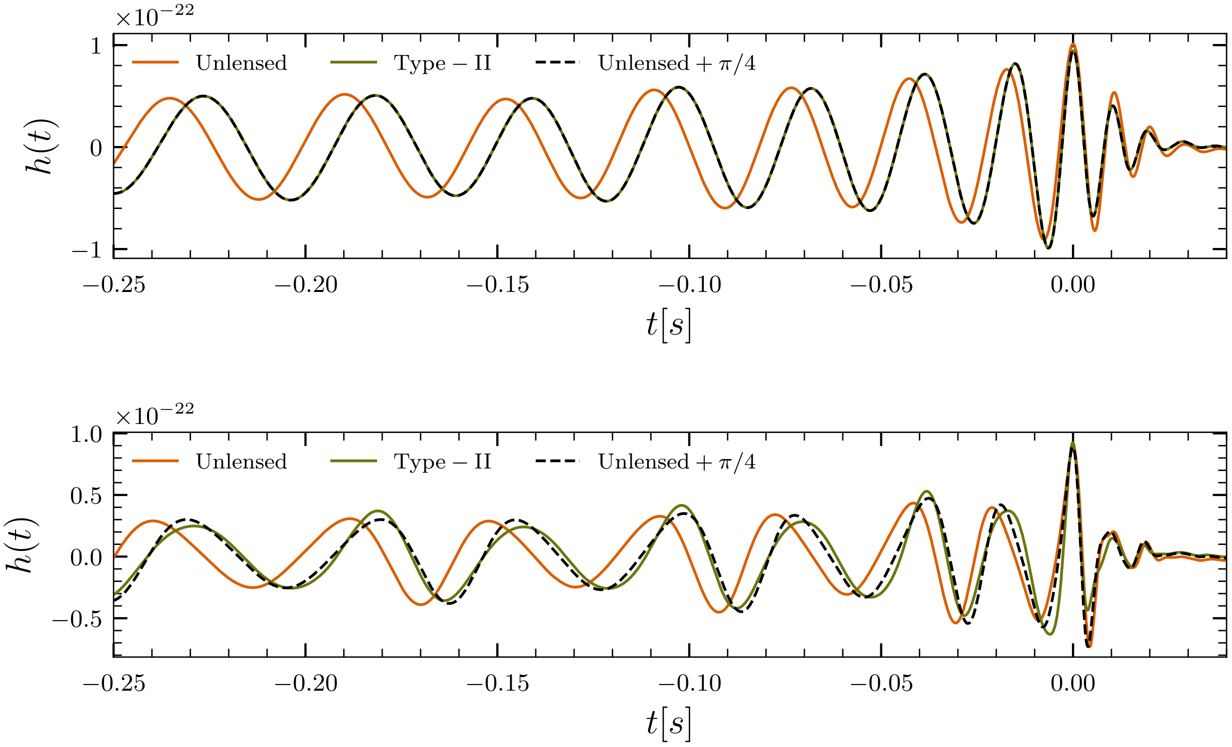

FIG. 1. The unlensed signal, the type-II signal, and the unlensed signal with a shift in the coalescence phase ϕ_c by $\pi/4$ for the parameters $M = 100M_\odot$, $q = 7$, $\iota = 0$ (top panel), and $\iota = \pi/3$ (bottom panel). For the zero inclination (top panel), i.e., when mainly 22 mode contributes, the GR signal reproduces the type-II image signal very well by adjusting its coalescence phase, while for high inclination (bottom), the type-II signal is not reproduced by the GR signal fully; i.e., there are additional distortions left.

correct template is not used. Below, we discuss the simulations' details to address these questions.

B. Simulations and Bayesian inference

Measurement of parameters from a GW signal amounts to estimating the posterior probability density function (PDF) $p(\theta|d)$, where θ is the set of parameters that describes a GW signal and d is the data stream from the interferometers in the network. According to Bayes theorem, the posterior PDF is given by

$$p(\theta|d) = \frac{\mathcal{L}(d|\theta)\pi(\theta)}{\mathcal{Z}}. \tag{18}$$

Here, $\mathcal{L}(d|\theta)$ is the likelihood function of the data given the parameters, $\pi(\theta)$ is the prior distribution for the parameters, and the normalization factor Z is the evidence, given by

$$Z = \int \mathrm{d}\theta \mathcal{L}(d|\theta)\pi(\theta). \tag{19}$$

The evidence can be thought of as the likelihood function marginalized over all the parameters. The evidence is not a useful quantity by itself but is very useful while comparing different models or hypotheses describing the data. In the context of this work, the two hypotheses that we consider are

A: the signal is unlensed;

B: the signal is type-II lensed.

In order to understand which hypothesis fits the data better, we formulate the Bayes factor $\mathcal{B}^{\text{type-II}}_{\text{unlensed}}$, which is defined as the ratio of the evidences of the two hypotheses:

$$\mathcal{B}^{\text{type-II}}_{\text{unlensed}} = \frac{Z_{\text{type-II}}}{Z_{\text{unlensed}}} \tag{20}$$

$$\Rightarrow \ln\mathcal{B} = \ln\mathcal{B}^{\text{type-II}}_{\text{unlensed}} = \ln Z_{\text{type-II}} - \ln Z_{\text{unlensed}}. \tag{21}$$

We simulate type-II image strains using Eq. (2) for total mass $M = m_1 + m_2 \in \{30, 70, 100, 140\}M_\odot$, mass ratio $q = m_1/m_2 \in \{2, 3, 5, 7, 10\}$, and inclination $\iota \in \{\pi/6, \pi/4, \pi/3, 5\pi/12, \pi/2\}$ of the nonspinning BBHs. We scale the luminosity distance of these injections to signal-to-noise ratios (SNRs), ρ, of 20 and 50 in a network with the LIGO-Hanford and LIGO-Livingston detectors at the Advanced LIGO sensitivity and the Virgo detector at the Advanced Virgo sensitivity [4]. We choose a realization of the detector noise that is exactly zero at all frequencies (called the "zero-noise" realization); this can be thought of as the most probable realization of the noise. This choice allows us to isolate the effects of waveform systematics on parameter estimation from the noise systematics. However,

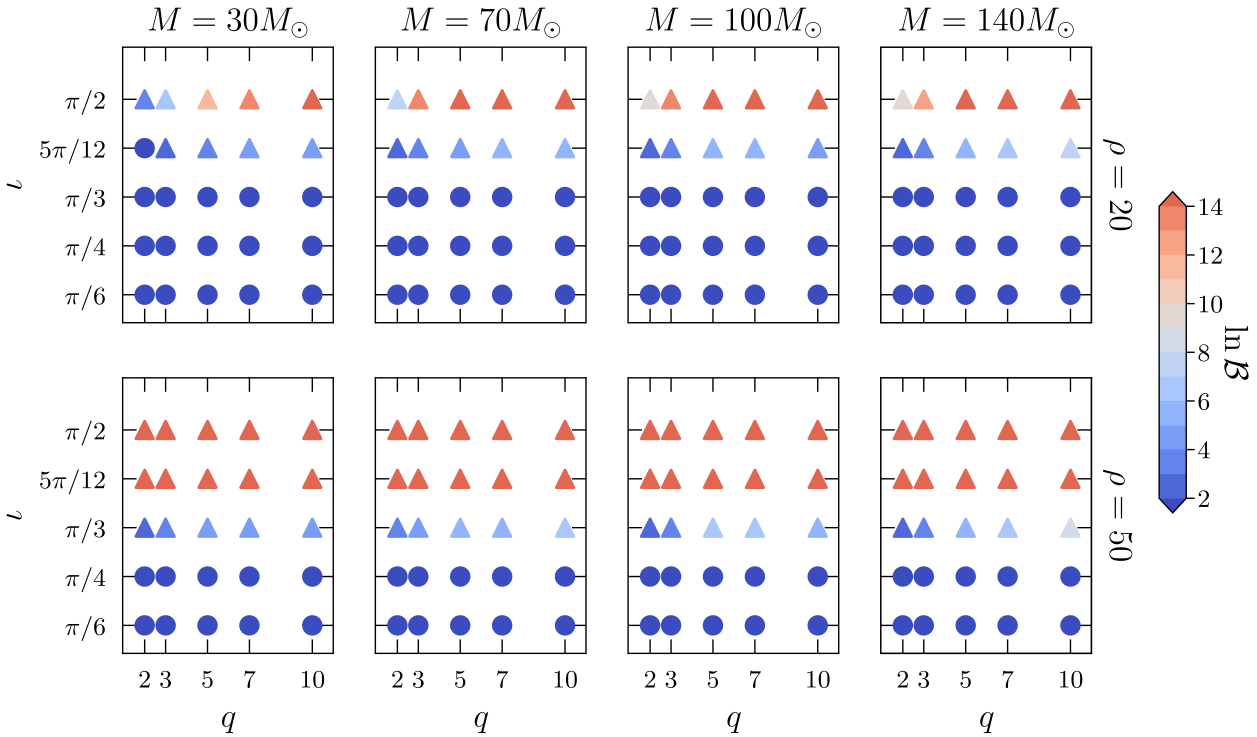

FIG. 2. Type-II lensed BBH injections with a network SNRs $\rho = 20$ (upper row) and $\rho = 50$ (lower row) shown in the $\iota - q$ plane for different total masses. The color bar shows the ln Bayes factor ($\ln\mathcal{B}$) between the type-II and the type-I recoveries. Injections which cross our threshold of $\ln\mathcal{B} \geq 2$ are plotted using triangles (i.e., distinguishable image types), while the others are plotted using circles.

a fully rigorous analysis would require adding a nonzero noise realization to these injections to make it directly relevant for the LIGO-Virgo observations. We leave this for future studies. Nevertheless, the SNRs (such as 50) considered in our work are expected to be high enough to minimize the effect of noise systematics in our results.

We perform full Bayesian parameter estimation on these injections (simulations) using type-I [Eq. (14)] and type-II [Eq. (15)] templates, keeping the priors on the source parameters the same between the recoveries for each injection. The priors we choose are uniform in the detector-frame chirp mass[6] and the mass ratio of the binaries, uniform in comoving volume for the luminosity distance, and uniform in sky location and inclination of the binaries. The parameter estimation runs are performed using BILBY and BILBY_PIPE [42,43] coupled with the dynamic nested sampler DYNESTY [44]. We use IMRPhenomXHM [45] as our waveform approximant for the runs; this approximant contains the 33, 44, 21, and 32 modes of the gravitational-wave signal in addition to the dominant 22 mode.

III. RESULTS

Figure 2 shows the Bayes factor between the type-II and type-I recoveries of type-II injected BBH signals at $\rho = 20$ and 50, respectively, for various total masses. We choose a threshold of $\ln\mathcal{B} = 2$ for the distinguishability of the type-II recovery against the type-I recovery of type-II injected signals [46,47]. Choosing a higher threshold for the distinguishability would require the lensed events to be observed at higher SNRs keeping other parameters fixed. The triangle shapes in Fig. 2 denote the signals which pass this threshold. We can see that at $\rho = 20$, independently of the total mass and the mass ratio, when the inclination $\iota \gtrsim 5\pi/12$, the type-II image signals become distinguishable from the type-I (or the unlensed) signals. At higher SNRs, e.g., $\rho = 50$, even less inclined binaries ($\iota \sim \pi/3$) will allow us to distinguish the lensed signals from the unlensed ones. This is because, at higher SNRs, the effect of HMs is more significant. Since $\ln\mathcal{B} \sim \rho^2$, we expect that, at even higher SNRs (e.g., 100 or larger), even smaller inclinations ($\sim\pi/4$) should allow us to distinguish the type-II images. This means that third-generation detector networks, where SNRs of $\sim$100 could be typical, would easily allow us to distinguish the type-II images even when the inclination is low. This prediction is also consistent with results from Ref. [7]. Although higher inclinations permit better measurement of type-II images, they are intrinsically less detectable; we note that $\iota \gtrsim 5\pi/12, \pi/3, \pi/4$ make up $\sim 5\%, 14\%, 34\%$ of the total detectable (lensed or unlensed) population of sources, respectively, based on the detected distribution of inclinations $p_{\rm det}(\iota) \sim (1 + 6\cos^2\iota + \cos^4\iota)^{3/2}\sin\iota$ [48].

---

[6] The chirp mass $\mathcal{M}$ is a mass parameter which describes the inspiral part of the BBH signals at leading order.

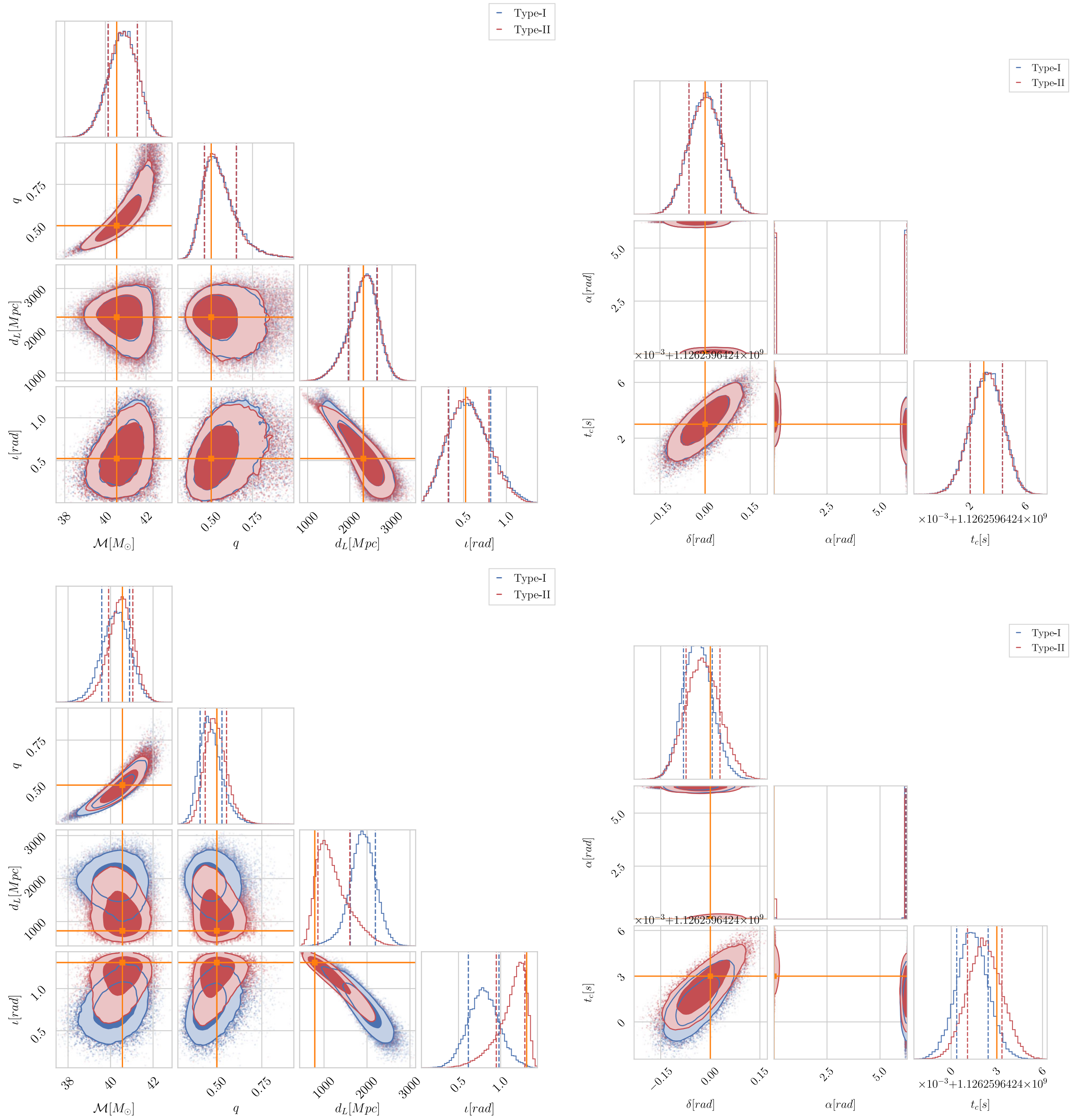

FIG. 3. Top row: the recovery of source parameters of an injected type-II signal using type-I (blue) and type-II (red) templates for $q = 2$, $M = 100M_\odot$, $\rho = 20$, and $\iota = \pi/6$. The plots show recovery of chirp mass $\mathcal{M}$, mass ratio q, luminosity distance d_L, inclination ι, sky locations δ (dec) and α (RA), and time of arrival t_c in the geocenter frame. The orange lines show the injected value. There is no appreciable difference between the posterior distributions for both the recoveries due to the low inclination and small SNR in the higher modes. Bottom row: the recovery of source parameters of an injected type-II signal using type-I (blue) and type-II (red) templates for $q = 2$, $M = 100M_\odot$, $\rho = 20$, and $\iota = 5\pi/12$. There is now a bias in the inclination and the distance, and the injected value is not recovered within 1σ. The bias in the distance also biases the recovery of the source frame masses. There are also some insignificant biases in the recovery of the sky locations and time of arrival.

For the distinguishable type-II image signals, we then explore the effect on the recovery of source parameters if they are recovered with type-I image (or, equivalently, unlensed) templates. The top row in Fig. 3 compares the recovery of an injected type-II image having $\rho = 20$, $M = 100M_\odot$, $q = 2$, and $\iota = \pi/6$ with both type-I and type-II templates. We see that the injected values lie well within the posterior PDFs for both recoveries, and there are

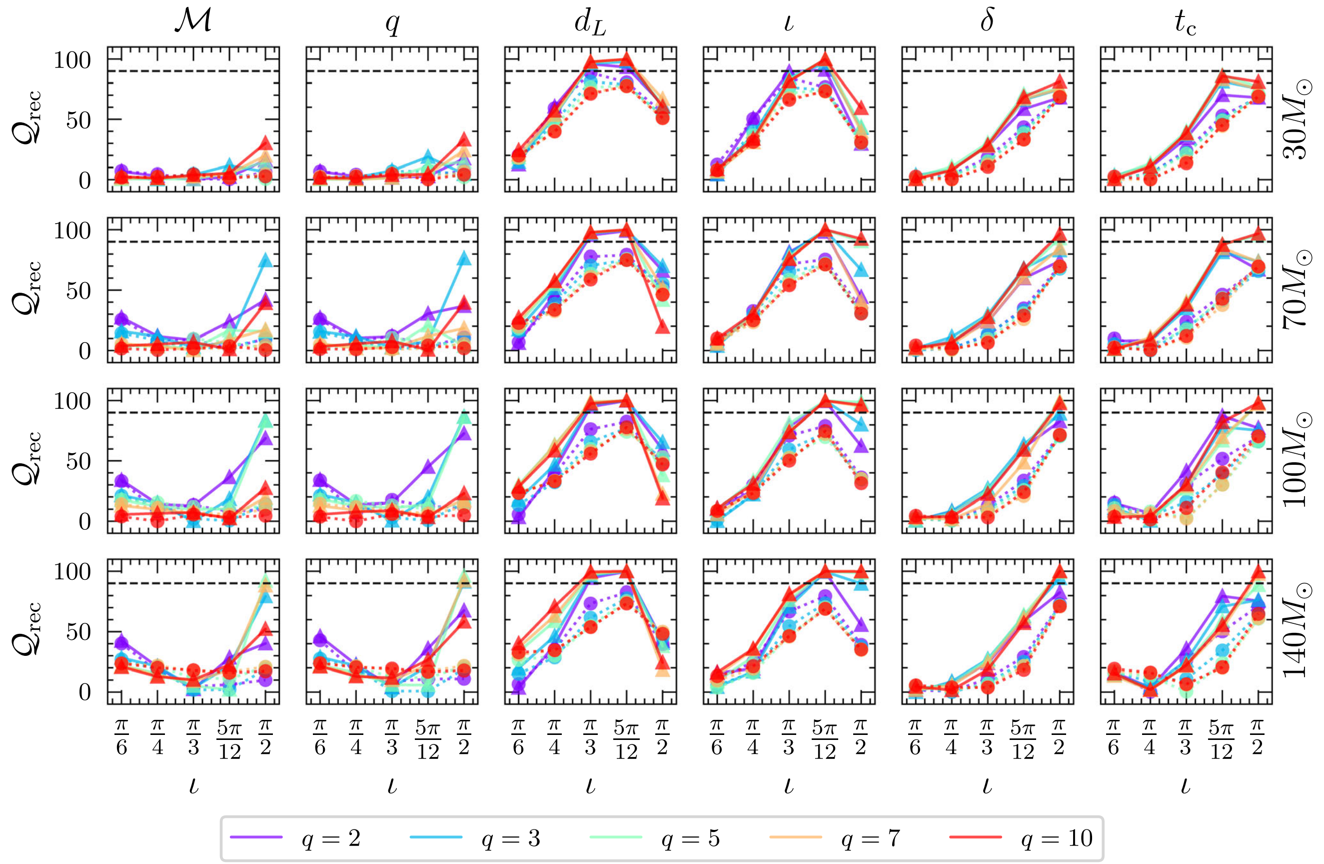

FIG. 4. Each panel shows the quantiles ($\mathcal{Q}_{\rm rec}$) of the injection value recoveries against the inclination angle (ι) of the injected BBH systems for a given total mass (M) (labeled on the right side of the panel) and SNR $\rho = 20$. The injections are the type-II lensed nonspinning BBH signals, and the recoveries are with the type-I template (solid lines) and the type-II template (dashed lines), accounting for the additional phase shift of $\pi/4$. At the top of the first panel, we label the parameters of the BBH systems that we are interested in. In each plot, the different colors denote the different mass ratios of the BBH systems. A lower quantile value denotes a more accurate inference of a parameter. The anomalous dips in $\mathcal{Q}_{\rm rec}$ at high values of ι are due to bimodalities in the recovery of t_c, ι, and δ at these values. We investigate these further in the Appendix.

no discernible differences between the two recoveries. However, increasing ι to $5\pi/12$ (bottom row in Fig. 3) keeping the other parameters fixed causes the injected masses, distance, and inclination values to lie in a region with low posterior probability if the recovery is made with a type-I template. This shows that the distortions in the waveform can cause significant biases in parameter estimation in certain regions of the parameter space. We investigate this further in Figs. 4 and 5, where we show results of recoveries with type-I image templates [Eq. (14)] denoted by solid lines and with type-II image templates [Eq. (15)] denoted by the dashed lines at SNR of 20 and 50, respectively, for different total masses of the type-II injected signals. On the y axis, we show the quantiles $\mathcal{Q}_{\rm rec}$ of the recovery of the injected values for the significantly affected parameters. For example, a $\mathcal{Q}_{\rm rec} = 90\%$ denotes that the injected value of the parameter is recovered at a value that forms one edge of the 90% posterior area; in other words, the injection value is recovered in the tail of the posterior. Such a case would represent a type-II signal which would provide a biased estimate of this parameter upon recovery with the unlensed template.

We can see from Fig. 4 that, at $\rho = 20$, for the type-II signals with lower total mass ($M = 30M_\odot$), the intrinsic parameters chirp mass $\mathcal{M}$ and mass ratio q are recovered at nearly the exact quantiles; i.e., the phase shift does not affect their recoveries. This could be because, as explained before, the HMs are not very relevant for the inspiral-dominated signals at low SNRs. At higher SNRs, however, the difference between the quantiles of their recoveries becomes significant at high inclination angles ($\iota \gtrsim 5\pi/12$) (Fig. 5). At such high SNRs, for higher total mass systems, the differences become significant even at the inclination $\iota \sim \pi/3$. This value of the inclination would further decrease with increasing SNR. We thus expect that the chirp mass and mass ratio would be affected significantly for the 3G detectors when $\rho \sim 100$ or greater could be achievable. We note that, even at $\rho = 50$, there are multiple binaries for which the quantiles of the chirp mass and mass

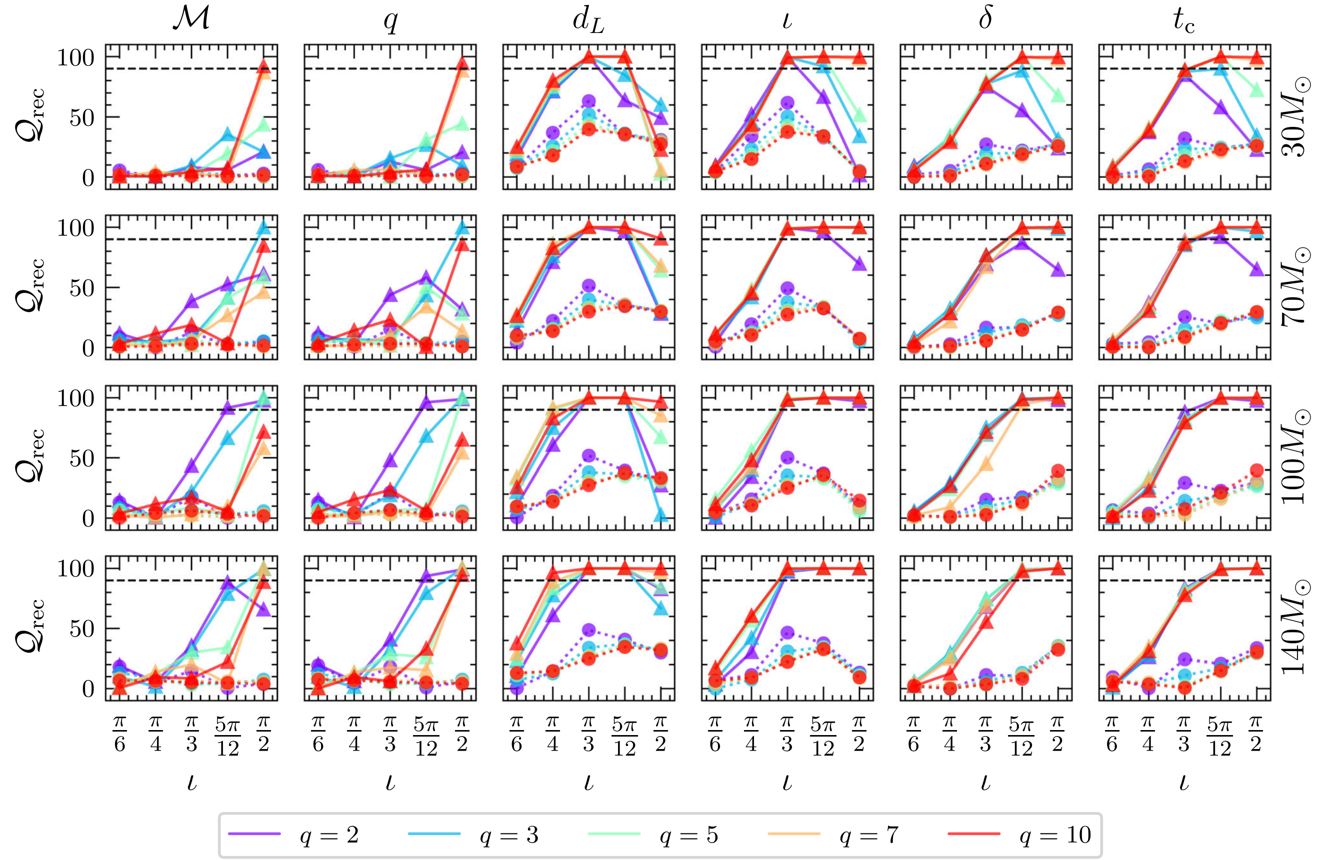

FIG. 5. The same as Fig. 4 but at $\rho = 50$.

ratio recoveries exceed 90%, and, thus, their estimates are completely biased (see Fig. 5).

The inference of the distance (d_L) and the inclination also get affected significantly at higher SNRs. At lower SNR (Fig. 4), there is not much difference between their recovery quantiles. However, the quantiles get pushed beyond 90% for a range of inclination angles ($\pi/3 \lesssim \iota \lesssim 5\pi/12$). At higher SNR (Fig. 5), on the other hand, the binaries even with the inclination angle of $\sim\pi/4$ face significant differences. We also find that the declination (δ) and coalescence time (t_c) are affected significantly at higher SNR. We can see from Fig. 5 that higher total mass systems with the inclination angle of $\sim\pi/3$ onward have completely biased estimates of these parameters. Again, increasing the SNRs further would lower the inclination at which parameters get biased further. We thus expect that most of the type-II lensed events in the 3G era will undergo biased estimates of these quantities, most notably the sky location.

We note that there are some seemingly anomalous features at $\iota = \pi/2$ in Figs. 4 and 5, where the value of $\mathcal{Q}_{\rm rec}$ drops as compared to $\iota = 5\pi/12$. These occur due to bimodalities in t_c, δ, and ι posteriors (see the Appendix for more details), thus rendering $\mathcal{Q}_{\rm rec}$ to be an insufficient quantifier for the bias at $\iota = \pi/2$.

IV. CONCLUSION AND FUTURE WORK

Strong lensing produces three types of images: type-I, type-II, and type-III, corresponding to the minima, saddle, and maxima, respectively, of the total arrival time of the lensed GWs. While type-I and -III images do not affect the frequency profiles of the unlensed BBH signals, the type-II image can, depending on the morphology of the signals. For example, if the unlensed BBH signals have support for HMs, precession, eccentricity, or any combination of these, the type-II image strains would receive additional distortions due to the phase shift ($\pi/2$) caused by strong lensing. In this work, we explored the possibility of identifying type-II lensed signals using these distortions in the observed signals.

Using a set of full parameter estimation recoveries for type-II lensed injections on a varied parameter space, we showed that it would be possible to ascertain the type-II nature of the most lensed BBH signals at high SNRs. This becomes very relevant for the 3G detectors and beyond, where such high SNR events could be frequently expected. This study implies that we should be able to tell if an event is type-II lensed or not just by the observation of a single image.

We then showed that the identifiable type-II images, which are of our interest here, will have sufficient distortions caused by the lensing phase shift $\pi/2$ that, when they are recovered with type-I image templates, would recover significantly biased parameters of the underlying BBH signals. We quantified these biases for a range of inclinations, total mass, and mass ratios of the binary. Our results suggest that the recovery of parameters such as the chirp mass, mass ratio, coalescence time, luminosity distance, inclination, and sky position of the binary becomes significantly biased. Since the first-cut search for lensed pairs involves demanding consistency between the sky positions of the images, we suggest that parameter estimation should be performed using type-II templates on all signals because, *a priori*, we would not know the nature of the image types as well as the parameters of the signals.

In this work, we have considered nonspinning quasicircular BBH signals to concentrate on the effects of only including higher harmonics of the radiation. Extending this study to generic spinning BBH signals with eccentricity would be natural. We, however, expect that precession and/or eccentricity would cause similar biases [26]. We have already verified this from a few precessing BBH type-II injections, but a thorough study will shed more light on this. We also have not considered the impact of noise systematics on our ability to identify type-II lensed signals. We leave these investigations for future work, along with an exploration of the detectability of these effects for a population of simulated sources.

ACKNOWLEDGMENTS

We thank Jose Maria Ezquiaga, Justin Janquart, and Otto Hannuksela for discussions. We also thank Bala Iyer, Parameswaran Ajith, and other members of the Astrophysical Relativity group at ICTS for feedback and Sanskriti Chitransh for a careful reading of the draft. Computations were performed on the Alice cluster at ICTS. A. V.'s research is supported by the Department of Atomic Energy, Government of India, under Project No. RTI4001. This work makes use of NumPy [49], SciPy [50], Matplotlib [51], JUPYTER [52], DYNESTY [44], BILBY [42], PyCBC [53], LALSuite [54], and PESummary [55] software packages.

APPENDIX: INVESTIGATING PATTERNS IN THE BIAS

For some cases in Figs. 4 and 5, there are anomalous dips in the bias (quantified by $\mathcal{Q}_{\rm rec}$) at $\iota = \pi/2$. We investigate these below.

In order to illustrate the causes of these dips, we show the corner plot of source parameter recovery for a type-II injection with $q = 2$, $M = 70M_{\odot}$, $\rho = 50$, and $\iota = \pi/2$ with both type-I and type-II templates (Fig. 6). The posteriors obtained with the type-II template do not show any anomalous features, and the injection values lie near the peak of the posterior. However, this is not the case for type-I recovery. The first thing to note is that the t_c posterior is bimodal, thus also causing the δ posterior to be bimodal, since there is a correlation between the two parameters. This is perhaps not too surprising, since, as we have shown earlier, type-II effects distort the waveform away from GR considerably. One of the modes in the $t_c - \delta$ plane includes the injected value, while the other is far away from it. This bimodality also effectively broadens the region where the posterior has significant support, thus causing the $\mathcal{Q}_{\rm rec}$ to be shifted to lower values. This is the reason for the anomalous behavior seen at $\iota = \pi/2$, and one can also see that a similar argument holds for the recovery of ι as well. On the other hand, the d_L posterior peaks at the injected value, but the posterior width is larger than that in the type-I recovery case. This, again, causes a decrease in the value of $\mathcal{Q}_{\rm rec}$ estimated for the d_L parameter. The points noted above show that $\mathcal{Q}_{\rm rec}$ is not a good enough quantifier of the bias for these edge cases.

We have also checked that the likelihood values for samples at both modes are very similar. To check whether the waveforms themselves at these two modes are similar and to ensure sanity of the likelihood calculation and the sampling, we plot the frequency-domain amplitude and phase of the maximum likelihood waveforms (projected onto the LIGO-Hanford detector) from both the modes (Fig. 7). As one can clearly see, the waveforms match very well in the frequency domain.

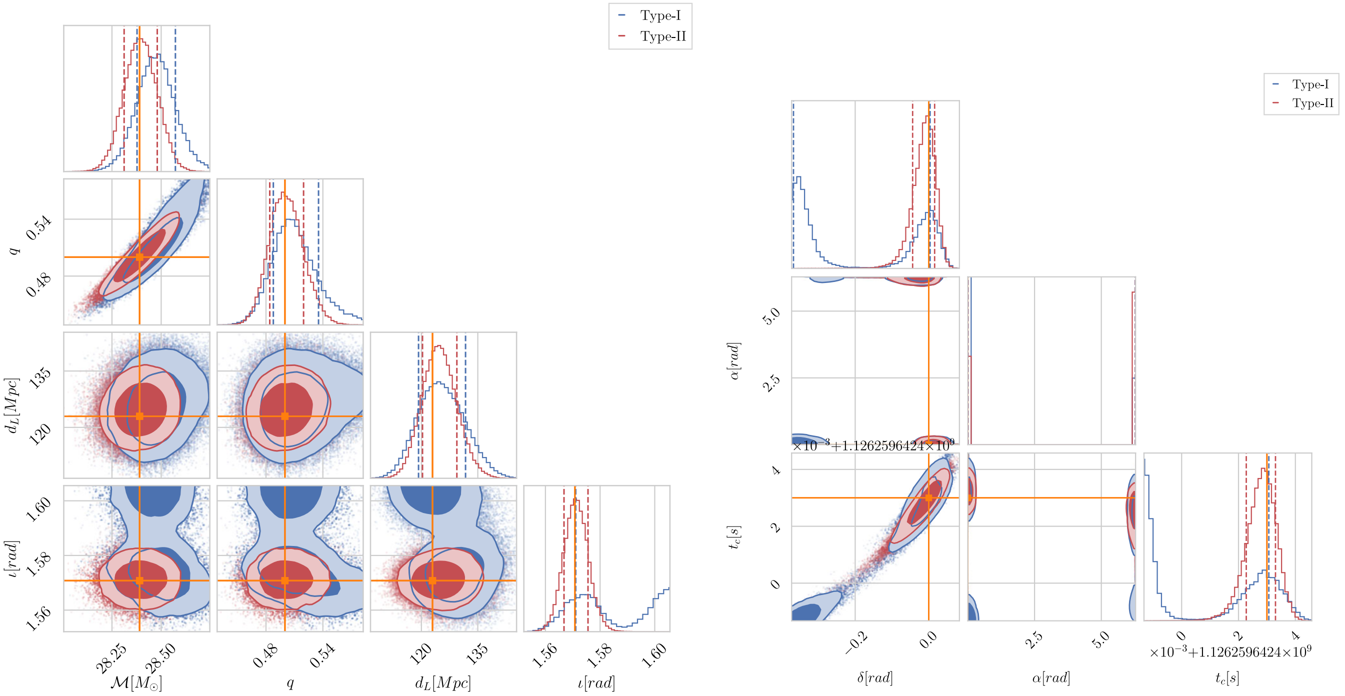

FIG. 6. The recovery of source parameters using type-I (blue) and type-II (red) templates for $q = 2$, $M = 70M_\odot$, $\rho = 50$, and $\iota = \pi/2$. The type-II recoveries are consistent with the injection values, but the type-I recoveries have correlated bimodalities t_c, δ, and ι. One of these modes is consistent with the injected values, while the other mode is far away from the injected values. The distance posterior does not have a significant bias with respect to the injected value; however, the width of the posterior is larger than that of the posterior in the type-II case.

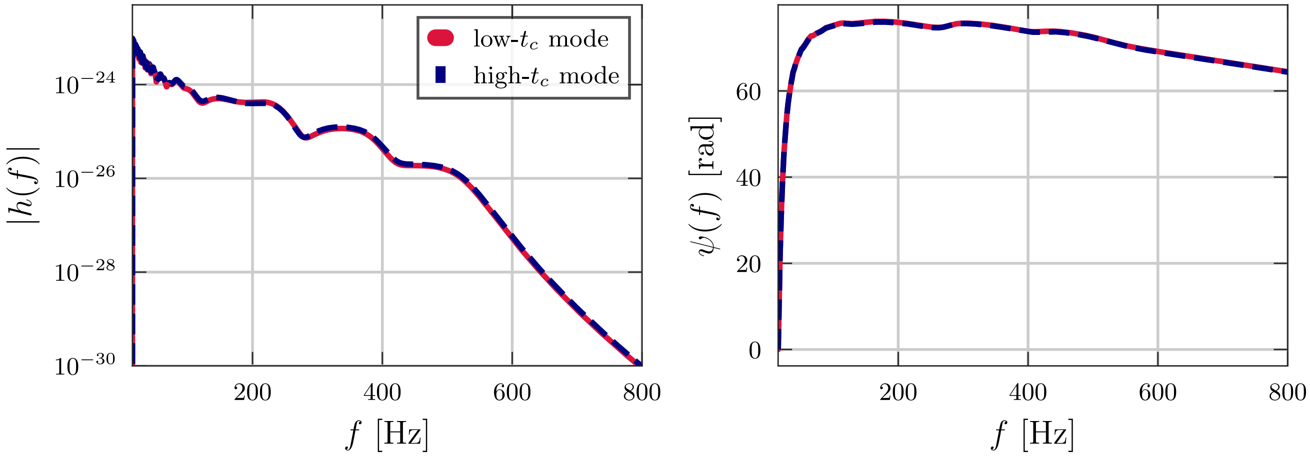

FIG. 7. Comparison of the waveform amplitude $|h(f)|$ and phase $\psi(f)$ (projected onto the LIGO-Hanford detector) for the maximum likelihood samples from the low-t_c and high-t_c modes. There is considerable agreement between the two waveforms.

[1] J. Aasi, B. P. Abbott, R. Abbott, T. Abbott, M. R. Abernathy, K. Ackley, C. Adams, T. Adams, P. Addesso, R. X. Adhikari, V. Adya, C. Affeldt, N. Aggarwal, O. D. Aguiar, A. Ain, P. Ajith, and J. Zweizig, Advanced LIGO, Classical Quantum Gravity **32**, 074001 (2015).

[2] F. Acernese, M. Agathos, K. Agatsuma, D. Aisa, N. Allemandou, A. Allocca, J. Amarni, P. Astone, G. Balestri, H. Vocca, R. Ward, M. Was, L. W. Wei, M. Yvert, A. Zadro żny, and J. P. Zendri, Advanced Virgo: A second-generation interferometric gravitational wave detector, Classical Quantum Gravity **32**, 024001 (2015).

[3] R. Abbott *et al.* (LIGO Scientific, Virgo, and KAGRA Collaborations), GWTC-3: Compact binary coalescences observed by LIGO and Virgo during the second part of the third observing run, arXiv:2111.03606 [Phys. Rev. X (to be published)].

[4] B. P. Abbott *et al.* (KAGRA, LIGO Scientific, and Virgo Collaborations), Prospects for observing and localizing gravitational-wave transients with Advanced LIGO, Advanced Virgo and KAGRA, Living Rev. Relativity **21**, 3 (2018).

[5] Liang Dai, Tejaswi Venumadhav, and Kris Sigurdson, Effect of lensing magnification on the apparent distribution of black hole mergers, Phys. Rev. D **95**, 044011 (2017).

[6] Ken K. Y. Ng, Kaze W. K. Wong, Tom Broadhurst, and Tjonnie G. F. Li, Precise LIGO lensing rate predictions for binary black holes, Phys. Rev. D **97**, 023012 (2018).

[7] Yijun Wang, Rico K. L. Lo, Alvin K. Y. Li, and Yanbei Chen, Identifying type II strongly lensed gravitational-wave images in third-generation gravitational-wave detectors, Phys. Rev. D **103**, 104055 (2021).

[8] O. A. Hannuksela, K. Haris, K. K. Y. Ng, S. Kumar, A. K. Mehta, D. Keitel, T. G. F. Li, and P. Ajith, Search for gravitational lensing signatures in LIGO-Virgo binary black hole events, Astrophys. J. Lett. **874**, L2 (2019).

[9] R. Abbott *et al.* (LIGO Scientific and Virgo Collaborations), Search for lensing signatures in the gravitational-wave observations from the first half of LIGO–Virgo's third observing run, Astrophys. J. **923**, 14 (2021).

[10] J. Aasi *et al.* (LIGO Scientific Collaboration), Advanced LIGO, Classical Quantum Gravity **32**, 074001 (2015).

[11] F. Acernese *et al.* (Virgo Collaboration), Advanced Virgo: A second-generation interferometric gravitational wave detector, Classical Quantum Gravity **32**, 024001 (2015).

[12] A. Renske A. C. Wierda, Ewoud Wempe, Otto A. Hannuksela, L. éon V. E. Koopmans, and Chris Van Den Broeck, Beyond the detector horizon: Forecasting gravitational-wave strong lensing, Astrophys. J. **921**, 154 (2021).

[13] Yoichi Aso, Yuta Michimura, Kentaro Somiya, Masaki Ando, Osamu Miyakawa, Takanori Sekiguchi, Daisuke Tatsumi, and Hiroaki Yamamoto (KAGRA Collaboration), Interferometer design of the KAGRA gravitational wave detector, Phys. Rev. D **88**, 043007 (2013).

[14] T. Akutsu *et al.* (KAGRA Collaboration), Overview of KAGRA: Detector design and construction history, Prog. Theor. Exp. Phys. **2021**, 05A101 (2021).

[15] Bala. Iyer *et al.*, LIGO-India Technical Report No. LIGOM1100296, 2011.

[16] M. Saleem *et al.*, The science case for LIGO-India, Classical Quantum Gravity **39**, 025004 (2022).

[17] David Reitze *et al.*, Cosmic Explorer: The U.S. Contribution to gravitational-wave astronomy beyond LIGO, Bull. Am. Astron. Soc. **51**, 035 (2019).

[18] B. Sathyaprakash *et al.*, Scientific objectives of Einstein Telescope, Classical Quantum Gravity **29**, 124013 (2012); Classical Quantum Gravity **30**, 079501(E) (2013).

[19] M. Sereno, Ph. Jetzer, A. Sesana, and M. Volonteri, Cosmography with strong lensing of LISA gravitational wave sources, Mon. Not. R. Astron. Soc. **415**, 2773 (2011).

[20] Xuheng Ding, Marek Biesiada, and Zong-Hong Zhu, Strongly lensed gravitational waves from intrinsically faint double compact binaries—prediction for the Einstein Telescope, J. Cosmol. Astropart. Phys. 12 (2015) 006.

[21] Tessa Baker and Mark Trodden, Multimessenger time delays from lensed gravitational waves, Phys. Rev. D **95**, 063512 (2017).

[22] Otto A. Hannuksela, Thomas E. Collett, Mesut Çalışkan, and Tjonnie G. F. Li, Localizing merging black holes with sub-arcsecond precision using gravitational-wave lensing, Mon. Not. R. Astron. Soc. **498**, 3395 (2020).

[23] Srashti Goyal, K. Haris, Ajit Kumar Mehta, and Parameswaran Ajith, Testing the nature of gravitational-wave polarizations using strongly lensed signals, Phys. Rev. D **103**, 024038 (2021).

[24] Fei Xu, Jose Maria Ezquiaga, and Daniel E. Holz, Please repeat: Strong lensing of gravitational waves as a probe of compact binary and galaxy populations, Astrophys. J. **929**, 9 (2022).

[25] Liang Dai and Tejaswi Venumadhav, On the waveforms of gravitationally lensed gravitational waves, arXiv:1702.04724.

[26] Jose María Ezquiaga, Daniel E. Holz, Wayne Hu, Macarena Lagos, and Robert M. Wald, Phase effects from strong gravitational lensing of gravitational waves, Phys. Rev. D **103**, 064047 (2021).

[27] R. Kormann, P. Schneider, and M. Bartelmann, Isothermal elliptical gravitational lens models, Astron. Astrophys. **284**, 285 (1994).

[28] K. Haris, Ajit Kumar Mehta, Sumit Kumar, Tejaswi Venumadhav, and Parameswaran Ajith, Identifying strongly lensed gravitational wave signals from binary black hole mergers, arXiv:1807.07062.

[29] Srashti Goyal, D. Harikrishnan, Shasvath J. Kapadia, and Parameswaran Ajith, Rapid identification of strongly lensed gravitational-wave events with machine learning, Phys. Rev. D **104**, 124057 (2021).

[30] Mesut Çalışkan, Jose María Ezquiaga, Otto A. Hannuksela, and Daniel E. Holz, Lensing or luck? False alarm probabilities for gravitational lensing of gravitational waves, Phys. Rev. D **107**, 063023 (2023).

[31] Xiaoshu Liu, Ignacio Magana Hernandez, and Jolien Creighton, Identifying strong gravitational-wave lensing during the second observing run of Advanced LIGO and Advanced Virgo, Astrophys. J. **908**, 97 (2021).

[32] Rico K. L. Lo and Ignacio Magana Hernandez, Bayesian statistical framework for identifying strongly lensed gravitational-wave signals, Phys. Rev. D **107**, 123015 (2023).

[33] Justin Janquart, Otto A. Hannuksela, K. Haris, and Chris Van Den Broeck, A fast and precise methodology to search for and analyse strongly lensed gravitational-wave events, Mon. Not. R. Astron. Soc. **506**, 5430 (2021).

[34] Justin Janquart, Eungwang Seo, Otto A. Hannuksela, Tjonnie G. F. Li, and Chris Van Den Broeck, On the identification of individual gravitational-wave image types of a lensed system using higher-order modes, Astrophys. J. Lett. **923**, L1 (2021).

[35] Christian Baraldo, Akio Hosoya, and Takahiro T. Nakamura, Gravitationally induced interference of gravitational waves by a rotating massive object, Phys. Rev. D **59**, 083001 (1999).

[36] Roger Blandford and Ramesh Narayan, Fermat's principle, caustics, and the classification of gravitational lens images, Astrophys. J. **310**, 568 (1986).

[37] Yi Pan, Alessandra Buonanno, Michael Boyle, Luisa T. Buchman, Lawrence E. Kidder, Harald P. Pfeiffer, and Mark A. Scheel, Inspiral-merger-ringdown multipolar waveforms of nonspinning black-hole binaries using the effective-one-body formalism, Phys. Rev. D **84**, 124052 (2011).

[38] Ajit Kumar Mehta, Chandra Kant Mishra, Vijay Varma, and Parameswaran Ajith, Accurate inspiral-merger-ringdown gravitational waveforms for nonspinning black-hole binaries including the effect of subdominant modes, Phys. Rev. D **96**, 124010 (2017).

[39] Juan Calderón Bustillo, Sascha Husa, Alicia M. Sintes, and Michael Pürrer, Impact of gravitational radiation higher order modes on single aligned-spin gravitational wave searches for binary black holes, Phys. Rev. D **93**, 084019 (2016).

[40] Vijay Varma, Parameswaran Ajith, Sascha Husa, Juan Calderon Bustillo, Mark Hannam, and Michael Pürrer, Gravitational-wave observations of binary black holes: Effect of nonquadrupole modes, Phys. Rev. D **90**, 124004 (2014).

[41] Collin Capano, Yi Pan, and Alessandra Buonanno, Impact of higher harmonics in searching for gravitational waves from nonspinning binary black holes, Phys. Rev. D **89**, 102003 (2014).

[42] Gregory Ashton *et al.*, BILBY: A user-friendly Bayesian inference library for gravitational-wave astronomy, Astrophys. J. Suppl. Ser. **241**, 27 (2019).

[43] I. M. Romero-Shaw *et al.*, Bayesian inference for compact binary coalescences with BILBY: Validation and application to the first LIGO–Virgo gravitational-wave transient catalogue, Mon. Not. R. Astron. Soc. **499**, 3295–3319 (2020).

[44] Joshua S. Speagle, DYNESTY: A dynamic nested sampling package for estimating Bayesian posteriors and evidences, Mon. Not. R. Astron. Soc. **493**, 3132 (2020).

[45] Geraint Pratten *et al.*, Computationally efficient models for the dominant and subdominant harmonic modes of precessing binary black holes, Phys. Rev. D **103**, 104056 (2021).

[46] Harold Jeffreys, *The Theory of Probability*, Oxford Classic Texts in the Physical Sciences (Oxford University Press, New York, 1939).

[47] Robert E. Kass and Adrian E. Raftery, Bayes factors, J. Am. Stat. Assoc. **90**, 773 (1995).

[48] Bernard F. Schutz, Networks of gravitational wave detectors and three figures of merit, Classical Quantum Gravity **28**, 125023 (2011).

[49] Stefan van der Walt, S. Chris Colbert, and Gael Varoquaux, The NumPy Array: A structure for efficient numerical computation, Comput. Sci. Eng. **13**, 22 (2011).

[50] Pauli Virtanen *et al.*, SciPy 1.0–Fundamental algorithms for scientific computing in Python, Nat. Methods **17**, 261 (2020).

[51] J. D. Hunter, Matplotlib: A 2d graphics environment, Comput. Sci. Eng. **9**, 90 (2007).

[52] Thomas Kluyver, Benjamin Ragan-Kelley, Fernando Pérez, Brian Granger, Matthias Bussonnier, Jonathan Frederic, Kyle Kelley, Jessica Hamrick, Jason Grout, Sylvain Corlay, Paul Ivanov, Damián Avila, Safia Abdalla, Carol Willing (Jupyter Development Team), Jupyter notebooks—A publishing format for reproducible computational workflows, in *Positioning and Power in Academic Publishing: Players, Agents and Agendas*, edited by Fernando Loizides and Birgit Scmidt (IOS Press, Netherlands, 2016), pp. 87–90.

[53] Alex Nitz *et al.*, gwastro/pycbc: Release v2.0.1 of PyCBC (2022).

[54] LIGO Scientific Collaboration, LIGO Algorithm Library—LALSuite, free software (GPL) (2018).

[55] Charlie Hoy and Vivien Raymond, PESummary: The code agnostic parameter estimation summary page builder, SoftwareX **15**, 100765 (2021).